Research Article | Vol. 13, No. 11 / 1 Nov 2022 / Biomedical Optics Express 5585
Biomedical Optics EXPRESS

Finding intracellular lipid droplets from the single-cell biolens' signature in a holographic flow-cytometry assay

DANIELE PIRONE,[1,2,7,8] DANIELE G. SIRICO,[2,3,7] MARTINA MUGNANO,[2] DANILA DEL GIUDICE,[2,4] IVANA KURELAC,[5,6] BEATRICE CAVINA,[5,6] PASQUALE MEMMOLO,[2,9] LISA MICCIO,[2] AND PIETRO FERRARO[2]

[1]*Department of Electrical Engineering and Information Technologies, University of Naples "Federico II", via Claudio 21, 80125 Napoli, Italy*
[2]*CNR-ISASI, Institute of Applied Sciences and Intelligent Systems "E. Caianiello", Via Campi Flegrei 34, 80078 Pozzuoli, Napoli, Italy*
[3]*DICMaPI, Department of Chemical, Materials and Production Engineering, University of Naples Federico II", Piazzale Tecchio 80, 80125 Napoli, Italy*
[4]*Department of Mathematics and Physics, University of Campania "Luigi Vanvitelli", 81100 Caserta, Italy*
[5]*Department of Medical and Surgical Sciences (DIMEC), Centro di Studio e Ricerca (CSR) sulle Neoplasie Ginecologiche, Alma Mater Studiorum-University of Bologna, 40138 Bologna, Italy*
[6]*Centre for Applied Biomedical Research (CRBA), University of Bologna, 40138 Bologna, Italy*
[7]*contributed equally*
[8]*daniele.pirone@isasi.cnr.it*
[9]*pasquale.memmolo@isasi.cnr.it*

Abstract: In recent years, intracellular LDs have been discovered to play an important role in several pathologies. Therefore, detection of LDs would provide an in-demand diagnostic tool if coupled with flow-cytometry to give significant statistical analysis and especially if the diagnosis is made in full non-invasive mode. Here we combine the experimental results of in-flow tomographic phase microscopy with a suited numerical simulation to demonstrate that intracellular LDs can be easily detected through a label-free approach based on the direct analysis of the 2D quantitative phase maps recorded by a holographic flow cytometer. In fact, we demonstrate that the presence of LDs affects the optical focusing lensing features of the embracing cell, which can be considered a biological lens. The research was conducted on white blood cells (i.e., lymphocytes and monocytes) and ovarian cancer cells. Results show that the biolens properties of cells can be a rapid biomarker that aids in boosting the diagnosis of LDs-related pathologies by means of the holographic flow-cytometry assay for fast, non-destructive, and high-throughput screening of statistically significant number of cells.

1. Introduction

The introduction of biological sample as element in optics and photonics has opened new and unexplored horizons since its first conceiving and related experimental demonstration [1,2]. A biological living cell is not seen like only the investigation object anymore, but like a suitable element to realize various functionalities such as imaging [1,3], lithography [4], and photonic waveguide [5]. The significant advantage lies in the fact that biolenses are intrinsically full biocompatible [6–13]. In optical microscopy, a direct and real-time visualization of the sample and even more solutions are excogitated and investigated for improving the imaging performances. For example, new techniques are considered to overcome the optical diffraction limit and realize super-resolution imaging [14], e.g. microsphere-assisted techniques [15]. Unfortunately, usually such microspheres are not biocompatible, thus their biomedical application is limited. Instead,

#460204 https://doi.org/10.1364/BOE.460204
Journal © 2022 Received 1 Apr 2022; revised 12 May 2022; accepted 16 May 2022; published 4 Oct 2022

Biomedical Optics EXPRESS

the adoption of living cells as biolenses in optical devices opens the doors to intriguing trends for super-resolution imaging scopes [9,13]. In the recent years numerous biological samples have been investigated as active [1] or passive [5] optical elements in new bio-compatible photonic devices. The first known attempt in using a living cell as biolens was about red blood cells (RBCs) [1]. By means of interferometric optical technique, such as digital holography (DH), it was possible to tune focal lengths according to the RBCs' shape [1,6–8,10]. However, the lensing effect induced by a biological sample has been exploited to realize high-resolution imaging not only by using the whole cell structure [11], but also endogenous intracellular structures such as lipid droplets (LDs) have been demonstrated to be useful at this purpose. In fact, it has been proved that LDs could act as intracellular micro-lenses for enhancing the real-time monitoring of sub-cellular structures by fluorescence microscopy [12]. The behavior of the whole cell and its intracellular structures as biolenses could be very helpful in biomedicine [1,16]. In particular, LDs are ubiquitous intracellular organelles mainly found in the cytoplasm of most eukaryotic cells [17,18], having distinctively higher RI, up to 1.48 [19]. Although they have long been regarded as storage organelles, recently their dynamic role in many cellular activities has been discovered, even if the underlying mechanism has not yet been fully understood [20,21]. In particular, LDs supply a defence activity against external stress conditions and their variations have been proved to influence many cellular processes [20,22–24]. For this reason, LDs are expected to be biomarkers for some diseases in which they are involved, such as diabetes [25], atherosclerosis [26], fatty liver disease [27], pathogen infections [28], neurodegenerative diseases [29] and cancer [30–33]. Moreover, it has been shown that during an inflammation process, the number and size of LDs remarkably increase in immune cells [23,28,34–36]. Very recently, this property has been verified inside monocytes from COVID-19 affected patients [37], thus suggesting their possible involvement in the SARS-CoV-2 pathogenesis [38]. Therefore, methods capable to provide a fast detection of LDs inside single cells are strongly requested in order to aid biomedical diagnostic applications. Currently, transmission electron microscopy (TEM) and fluorescent microscopy (FM) are the most used technologies for LDs investigation [39,40]. However, despite its high-resolution imaging, the TEM technique has strong limitations in terms of high-throughput, since only small regions of the cell can be studied with not very simple sample preparation procedures. Instead, the FM imaging can better answer to the high-throughput need as it can be used also in flow-cytometry. However, to make visible LDs, fluorescent dyes must be employed, which can damage the cells (photodamaging/phototoxicity) or alter their imaging (photobleaching). Thus, label-free and quantitative phase imaging (QPI) can be a useful tool for such scope, as demonstrated in Refs. [41–45] in which single-cell QPI systems in flow cytometry with extremely high-throughput and subcellular resolution allow to accurate screening of LDs in microalgal cells. In DH the cells are analysed usually through 2D images thanks to the light interference principles [46]. Moreover, the DH numerical refocusing capabilities have made possible the realization of DH flow cytometers [47]. By means of a suitable numerical processing, the quantitative phase map (QPM) can be extracted from the corresponding digital hologram. In QPI, exogenous stain agents can be avoided since the imaging contrast is provided by the refractive index (RI) contrast spatial distribution of the cell coupled to its morphology [41]. Therefore, a QPM is dense of quantitative information about the imaged cell, related to its biophysical features (e.g., dry mass), and this property has opened to new promising biomedical tools [43–45,48]. Furthermore, the most powerful evolution of QPI is tomographic phase microscopy (TPM), which consists in retrieving the 3D RI spatial distribution of a single cell by collecting several QPMs at multiple viewing angles around it [49,50]. Recently, to increase the throughput of the conventional TPM and to provide an isotropic 3D reconstruction of suspended cells, we proposed the in-flow TPM technique [51–54], and we demonstrated its advantages in recovering the 3D RI spatial distribution of LDs inside a single suspended cell and in measuring their label-free 3D quantitative parameters [17,55].

Biomedical Optics EXPRESS

In this work we propose and proof a novel strategy based on DH microcopy for revealing in simple way the presence of intracellular LDs in each suspended living cell flowing along a microfluidic channel. LDs are detected by evaluating the lensing properties of the whole biolens (i.e. the hosting cell). In fact, we observed that the presence of intracellular LDs affects the focusing properties of the biolenses. As first step of our study, we performed an advanced numerical simulation combined to the in-flow TPM experiments in order to investigate this phenomenon. In particular, two living cell lines were considered. We examined A2780 ovarian cancer cells as positive case, i.e., cells with high amount of LDs [55], while we analyzed Jurkat T-lymphocyte white blood cells (WBCs) as negative case, i.e. as the model of a cell with low LDs number [56]. In fact, in case WBCs are in healthy conditions, LDs are not completely absent, but their number and size are low. When LDs have sizes comparable with the wavelength, they cannot be detected due to sensitivity of our system that depends on the trade-off between LDs size and axial resolution. For this reason, we considered Jurkat T-lymphocyte as negative case. Finally, another line of WBCs, i.e., human monocytes THP-1, has been recorded by the DH flow cytometer before and after the appearance of LDs, in order to test the ability of the proposed approach in correctly identifying the presence of LDs. Therefore, we demonstrate that the time and resource consuming 3D TPM reconstruction and the not trivial downstream segmentation of LDs can be avoided for the purpose of identifying them inside single flowing cells, since a much simpler and faster 2D DH flow cytometer can solve this same task by exploiting the LDs biolens features. We believe that, also thanks to the deep learning-based speeding-up of the holographic processing [57], the distinctive focalization properties of cells we shown here would be very helpful for a fast pre-screening about some important LDs-related pathologies. It is noteworthy that our system operates in flow-cytometry modality, which means analyzing large amounts of cells (e.g., overall in this investigation were studied more than 400 cells) thus providing in perspective the real chances to become a tool in support of clinic applications.

2. Materials and methods

2.1. Sample preparation

For these experiments we considered human ovarian cancer cell line A2780, THP-1 monocyte cell line and human Jurkat T-lymphocyte cell line. The cell lines were supplied by a third part. The base medium for these cell lines was RPMI 1640 Medium (Euroclone #ECB9006L), 2mM L-Glutamine (Lonza, Cat N.: BE17-605E) and 1% Penicillin/Streptomycin (Lonza, Cat N. DE17-602E). For the cancer and monocyte cells this medium was supplemented by 10% FBS (Euroclone #ECS5000L), whereas for the T-lymphocyte cells by 20% FBS, and both were maintained at 37°C in a humidified atmosphere with 5% CO2. A2780 cells support the adherent phenotype, while Jurkat and THP-1 cells support the suspension phenotype and were cultured in 25 cm^2 flasks. In order to prepare the A2780 sample, cells were washed twice with PBS 1× (Life technologies 10010023) and incubated with 1.5 mL of 0.05% trypsin–EDTA solution (Sigma, T4049-00ML) in incubator for 5 min. Then, they were detached and resuspended in a solution composed by PBS 1× and 10% FBS, so they were injected into the microfluidic channel at final concentration of 2×10^5 cells/mL. At the same time, T-lymphocytes and monocytes were harvested from their flasks and centrifuged for 5 min at 1000 rpm. They were resuspended in their medium to obtain a final cell concentration of 2×10^5 cells/mL. In all cases, Typan Blue solution 0.4% (Sigma T8154) was used to quantify the cells viability.

2.2. DH flow cytometer

For the digital recording of holograms, we employed an off-axis DH setup, based on a Mach-Zehnder optical interferometer. This arrangement grants an angle between the object and reference beam and decouples spatially the different diffraction orders in the Fourier space. A

Biomedical Optics EXPRESS

solid-state continuous wave laser source (Laser Quantum Torus 532) of wavelength $\lambda = 532$ nm emits the light beam which is split in object and reference beam by a polarizing beam splitter (PBS). Then, to adjust the splitting ratio of the two beams, two half-wave plates (HWPs) are placed in front of and behind the PBS. As depicted in Fig. 1(a), the object beam passes through the plane of the microfluidic channel where cells flow and rotate, then the scattered light is collected by a microscope objective (MO_1) and sent to a tube lens (TL_1). The reference beam follows a free path where passes through another microscope objective and a tube lens.

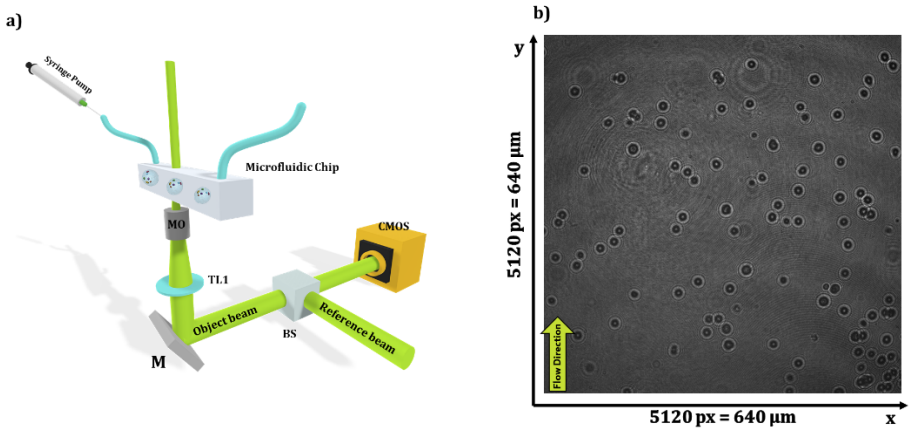

Fig. 1. DH experimental system. **(a)** Sketch of the DH flow cytometer. BS – beam splitter; M – mirror; TL – tube lens; MO – microscope objective; CMOS – camera. **(b)** Full FoV of a recorded digital hologram in which cells flow along the y-axis and rotate around the x-axis.

At the end of their paths, object and reference beams are combined by a beam splitter cube (BS) and their interference results in the hologram formation digitally recorded by a CMOS camera. The CMOS camera employed is a well performing camera (Genie Nano-CXP Camera) made of an array of 5120×5120 pixels, whose pixel size is $\Delta x = \Delta y = 4.5$ µm. This interferometric optical setup provides a magnification of $M = 36$, thus a field of view (FoV) of 640×640 µm^2 (see Fig. 1(b)) is observable with a lateral resolution equal to 0.5 µm. Biological samples are injected into a microfluidic chip (ChipShop Fluidic 138 10000107) by a controlled syringe pump (CETONI Syringe Pump neMESYS 290N) that grants a constant flow rate (75 nl/s) in laminar regime and a 360° cell rotation. Therefore, multiple views of the same cell are collected in few seconds since they are recorded along a fixed direction while cell is flowing and rotating.

2.3. DH numerical processing

The reconstruction of the DH sequence follows a well-defined pipeline to obtain the corresponding QPMs. The first step is the hologram demodulation where the real diffraction order is selected, centered and filtered in the Fourier space [46]. Then, a region of interest (ROI) with a single flowing cell is selected for each frame in the FoV. Each ROI is a demodulated sub-hologram that is propagated by means of the Angular Spectrum method [58] to refocus the complex amplitude. The research of the in-focus distance is based on the minimization of the Tamura coefficient (TC) calculated on the amplitude maps [59]. Generally, the in-focus QPMs are affected by aberrations induced mainly by optical elements of the interferometric setup. Among the different methods to compensate them [60], in this work we subtracted a reference hologram acquired without the specimen. The 2D windowed Fourier transform filtering [61] was used to denoise the QPMs and the PUMA algorithm to unwrap them [62]. Finally, once obtained all the QPMs of a sequence, they were combined to reconstruct the 3D tomogram by means of the Filtered Back Projection

Biomedical Optics EXPRESS

algorithm [51,53]. This procedure requires to know the rolling angle for each QPM, then a phase similarity method has been employed to retrieve them [53].

2.4. LDs as biolenses

In this section, we exploit tomographic reconstructions to assess the proposed method by simulating a realistic light propagation model through the 3D structure of a flowing cells with the aim to precisely characterize LDs. In particular, the DH flow cytometer shown in Fig. 1(a) has been exploited to reconstruct the 3D RI tomograms of the A2780 ovarian cancer cell and the Jurkat T-lymphocyte cell reported in Figs. 2(a, f), respectively, thanks to the in-flow TPM paradigm [44,46]. The A2780 cancer cell line has been chosen as positive case due to the presence of many large LDs inside [30], while the Jurkat T-lymphocyte WBCs have been selected as negative case since, in physiological conditions, the number and the size of their LDs are very low [36]. For this reason, in the isolevels representation of the tomographic reconstruction displayed in Figs. 2(b, g), the LDs are only visible in the A2780 cell, in which they have been segmented at the highest RIs (corresponding to the highest phase values in Fig. 2(a)) [55]. The Multi-Slice Beam Propagation (MSBP) forward model has been implemented to simulate the in-focus complex wavefront produced by the RI tomogram [63]. The simulated QPMs about the overall A2780 cell, the sole LDs segmented from the A2780 cell, and the Jurkat T-lymphocyte cell are shown in Figs. 2(c, d, h), respectively.

Moreover, the corresponding experimental QPMs numerically retrieved from the recorded holograms about the A2780 and the Jurkat T-lymphocyte cell are displayed in Figs. 2(e, i), respectively, to show the reliability of the MSBP method. Then, both the simulated and recorded in-focus complex wavefronts have been propagated at different distances along the optical z-axis by means of the Angular Spectrum method [58]. For each z position, the intensity of the propagated complex field has been considered. To deepen the effect due to the presence of LDs, within the QPMs in Figs. 2(c-e), the vertical lines passing for the maximum phase value found in the experimental QPM in Fig. 2(e) have been selected. In the same way, within the QPMs in Figs. 2(h, i), the vertical lines passing for the maximum phase value found in the experimental QPM in Fig. 2(i) have been selected. Hence, in Figs. 3(a-e), for each z propagation distance, we report the intensity values extracted respectively from the QPMs in Figs. 2(c-e, h, i) along the selected lines. It can be noted that the intensity mapping has a remarkable difference between the A2780 and lymphocyte case. In fact, in both the simulated and the experimental intensity mapping about the A2780 cell (see Figs. 3(a, c), respectively), there are small maximum values in the initial part of the optical z-axis (see the arrows before 10 μm), while they miss in both the simulated and the experimental intensity mapping about the Jurkat T-lymphocyte cell (see Figs. 3(d, e), respectively). These maximum regions are due to LDs that behave as biolenses. In fact, due to their smaller sizes, LDs focalize much before the entire cell in a distinguishable region within the intensity mapping because of their higher RIs. This is confirmed by the intensity mapping in Fig. 3(b) related to the sole LDs, in which the maximum areas are in the same z region as the overall cell in Figs. 3(a, c), as underlined by the arrow (note that spurious frequencies are related to the numerical error in the QPM simulation visible in Fig. 2(d) due to the high RI contrast between the LDs and the surrounding medium). Instead, in the Jurkat T-lymphocyte case, there is only the maximum region at longer z distances due to the focalization of the overall cell, which can be in turn considered as a bigger quasi-spherical lens. Note that the focalization of the overall cell is missing in the A2780 case since a lateral line has been selected. To consider the effect of the overall QPM without selecting a specific line, for each z distance we have computed the maximum intensity value of the propagated complex wavefront, thus obtaining the max-intensity curves in Figs. 3(f, g) about the analyzed A2780 and lymphocyte cell, respectively.

In Fig. 3(f) two main peaks are visible about the experimental cell, the farthest and highest one due to the focalization of the outer cell, and the closest and lowest one (before 10 μm) due to

Biomedical Optics EXPRESS

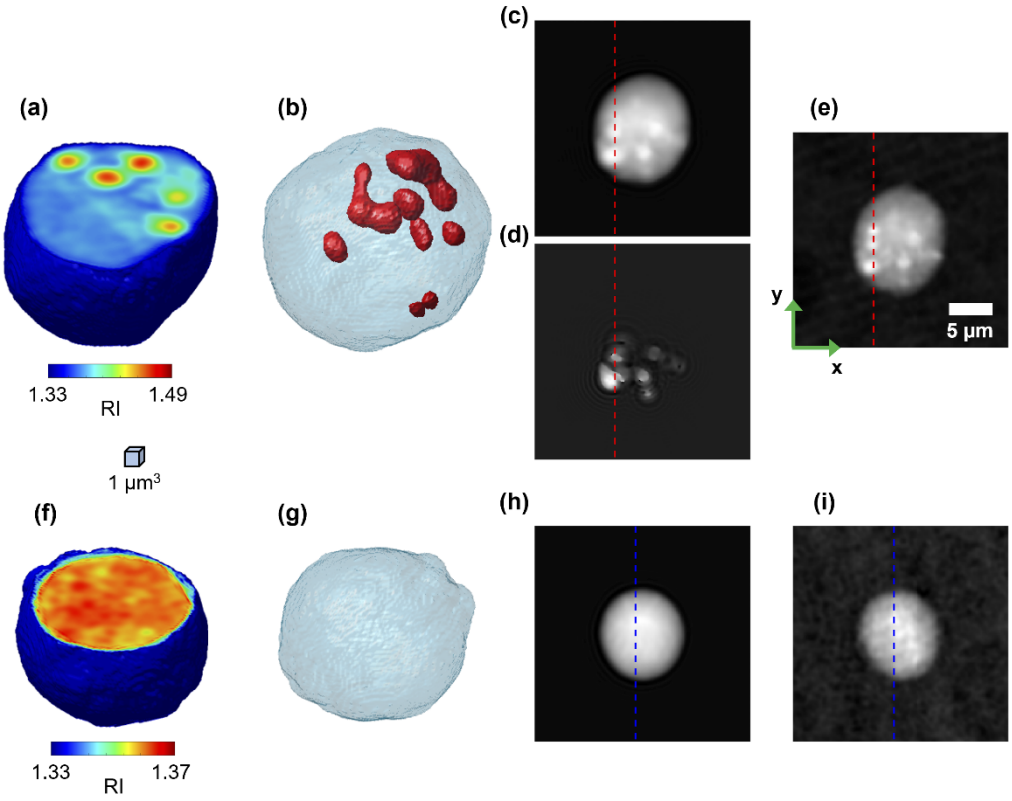

Fig. 2. Simulation of the light beam propagation through an experimental tomogram of an A2780 ovarian cancer cell (a-e) and a Jurkat T-lymphocyte WBC (f-i) obtained by the in-flow TPM. (a, f) Slice of the 3D RI tomogram reconstructed by means of the in-flow TPM method. **(b, g)** Isolevels representation of the reconstructed tomograms in (a, f), respectively. In (b), LDs have been segmented at the highest RIs (red volume). In (g), LDs are missing. **(c, d, h)** QPM simulated through the MSBP forward model starting from all the RIs in (a), the RIs of the sole segmented LDs in (a, b), and all the RIs in (f), respectively. **(e, i)** QPM numerically retrieved from the first frame of the experimental DH sequence used for reconstructing tomograms in (a, f), respectively. The experimental QPMs in (e, i) correspond to the simulated ones in (c, h), respectively. In (c-e), the red lines pass for the maximum phase value in (e). In (h, i), the blue lines pass for the maximum phase value in (i).

Biomedical Optics EXPRESS

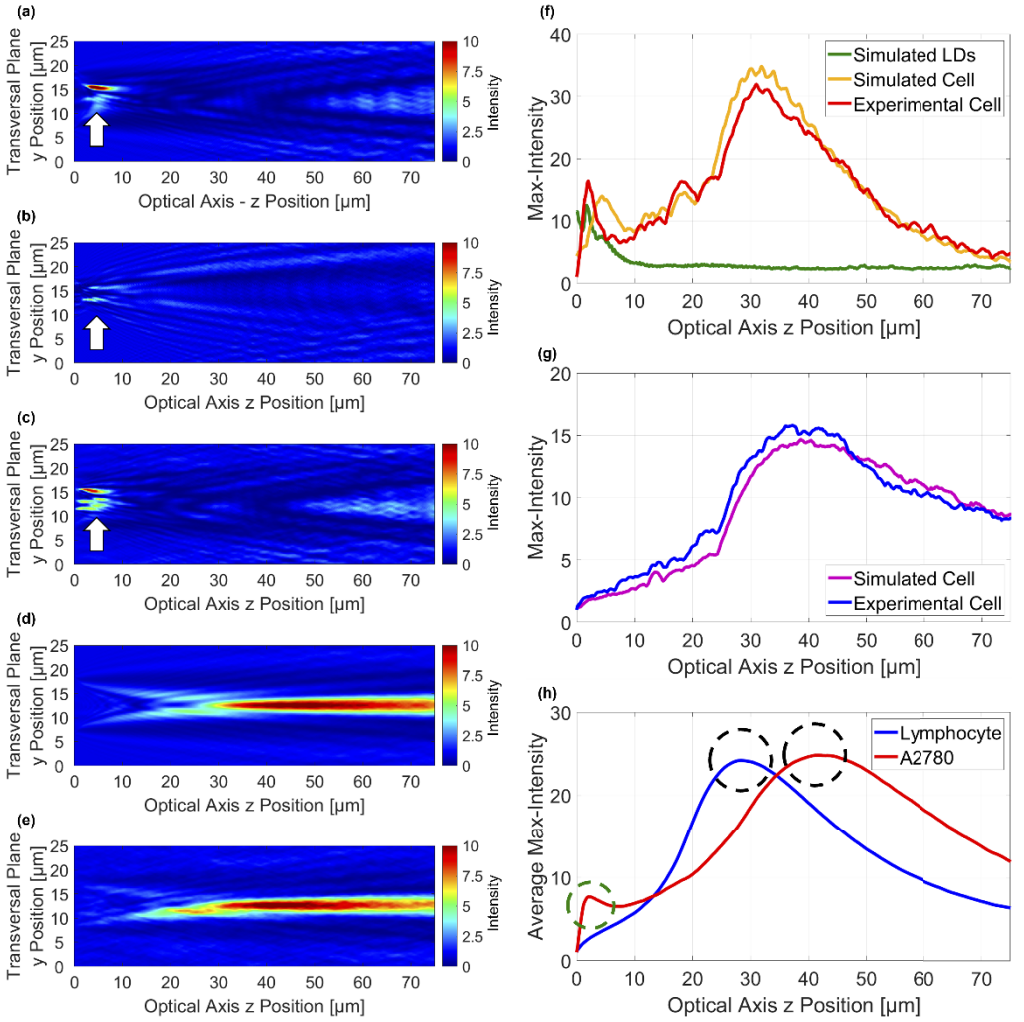

Fig. 3. Alteration of the focalization property of the whole cell due to the presence of LDs. (a-e) Intensity values of the complex wavefront propagated along the optical z-axis, taken from the y lines selected in Figs. 2(c-e, h, i) regarding the simulated QPM of the overall A2780 cell, the simulated QPM of the sole A2780 LDs, the experimental QPM of the overall A2780 cell, the simulated QPM of the overall Jurkat T-lymphocyte cell, and the experimental QPM of the overall Jurkat T-lymphocyte cell, respectively. Arrows in (a-c) highlight the perturbation of the cell biolens features by LDs. **(f, g)** Max-intensity of the complex wavefront propagated along the optical z-axis about the analyzed A2780 cell and Jurkat T-lymphocyte cell, respectively. **(h)** Average max-intensity computed among all the Jurkat T-lymphocyte cells (blue line) and A2780 cells (red line). The high peaks (black circles) are related to the focalization of the overall cell. The small peak (green circle) is related to the focalization of LDs.

Biomedical Optics EXPRESS

the perturbation introduced by LDs, as also confirmed by the max-intensity curve related to the sole LDs. Instead, in Fig. 3(g), only the farthest peak related to the focalization of the whole cell can be observed. Essentially, in order to summarize the concept behind the detection of LDs, it can be useful to consider that LDs are themselves biolenses and therefore the optical properties of the overall biological optical system consists in the whole cell (primary biolens) and a number of smaller embedded biolenses (i.e. intracellular LDs). It is important to underline that, the LDs detection accuracy is strictly related to the sensitivity of the max-intensity measures to provide the peak, as reported in Figs. 2(f-h). This sensitivity depends on the trade-off between LDs size and axial resolution, i.e. LDs having sizes comparable with the wavelength cannot be detected. This suggests that such biological-lens system is more complex in respect to the single lensing effect of the cell itself. Just for illustrative purpose, it can be useful to depict the composed biological-lens system as shown in Fig. 4, where the cell is the primary biolens while LDs affect the global focusing process.

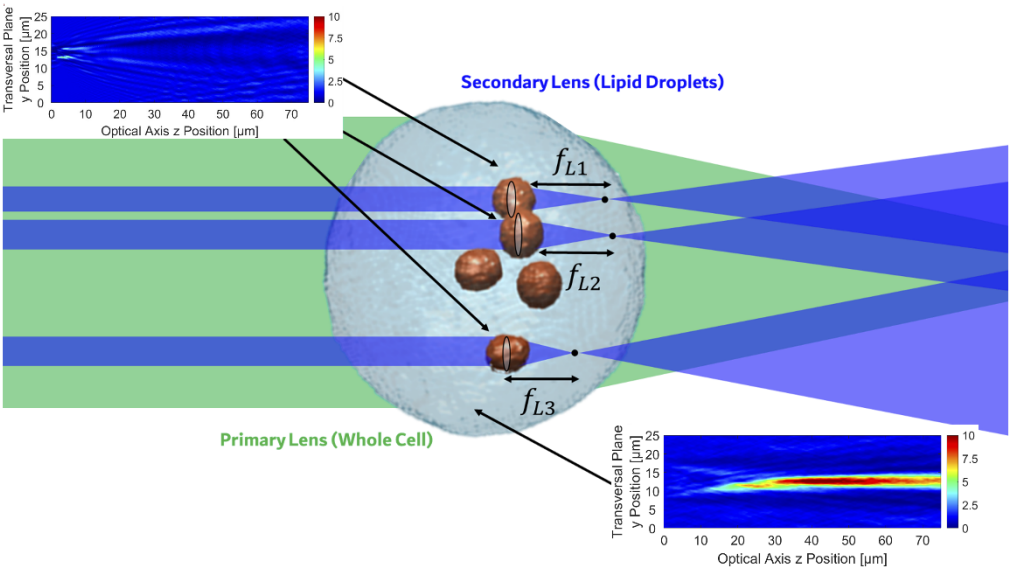

Fig. 4. Schematic representation of the optical system composed of cell and LDs. The outer cell act as the primary lens, the LDs act as secondary lenses with a much shorter focal length.

3. Results

To assess the perturbation introduced by the LDs to the biolens features of the whole cell, as summarized in Table 1, 537 QPMs of 202 Jurkat T-lymphocytes and 575 QPMs of 60 A2780 ovarian cancer cells have been recorded through the DH flow cytometer while flowing and rotating along the microfluidic channel. In Fig. 3(h), the max-intensity curves computed for each 2D QPM have been averaged inside the Jurkat T-lymphocyte cell line (blue) and the A2780 cell line (red), at the aim of analyzing the focalization property of these two populations on a greater number of cells. The two average max-intensity curves show again a maximum peak due to the focalization of the overall cell (black circles), while, as expected from the biological point of view, the smaller peak due to the presence of LDs is instead localized at the initial z distances only in the A2780 case (green circle). For this reason, we expect that the variation of the cell focalization property caused by LDs could be exploited for a fast detection of cells with LDs inside by means of a DH flow cytometer.

Biomedical Optics EXPRESS

Table 1. Dataset of Jurkat T-lymphocyte and A2780 ovarian cancer cells collected through the DH flow cytometer

	# QPMs	# Cells
Lymphocyte	537	202
A2780	575	60

At this aim, we consider again the Jurkat T-lymphocyte WBC and the A2780 ovarian cancer cell studied in Section 2.4, and in Fig. 5(a) we display the comparison between their max-intensity curves. As shown in Fig. 5(b), to deepen the perturbation due to LDs, we limit our analysis about the max-intensity curve only to the first 2 μm along the optical z-axis, since it is the region between the focal plane of the cell and the location of the LDs peak in the max-intensity curve. In fact, this region is expected to provide the best detection accuracy in the shortest possible time, since this is the region in which the difference between the cases with and without LDs (red and blue curve, respectively) is maximized, and at the same time the depth of the z-stack along which the QPM is numerically propagated by means of the Angular Spectrum formula is very small (i.e., the numerical z-scanning is fast). To avoid errors related to the different cell sizes and not to the presence of LDs, the two zoomed-in max-intensity curves have been normalized to their maxima in the range from 0 to 2 μm, thus obtaining the normalized max-intensity curves displayed in Fig. 5(c). As the maximum value of the zoomed-in max-intensity curve about the A2780 cell is much greater than the Jurkat T-lymphocyte one (see Fig. 5(b)), the average value of the normalized max-intensity curve about the A2780 cell is much smaller than the Jurkat T-lymphocyte one (see Fig. 5(c)).

Moreover, the presence of LDs leads to different slopes in the initial regions of the max-intensity curves. For this reason, the normalized max-intensity curves have been fitted through a 2^{nd} order polynomial, as reported in Fig. 5(d)). Hence, in order to characterize the normalized max-intensity curves reported in Figs. 5(c, d), two parameters have been considered, i.e., the average value and the quadratic coefficient of the 2^{nd} order polynomial fitting. In the scatter plot of Fig. 6(a), the QPMs of the recorded Jurkat T-lymphocyte and A2780 cells have been represented by means of their max-intensity average values and quadratic coefficients. Remarkably, these two parameters can provide a great separation between these two cell lines due to the presence or not of LDs, as also demonstrate by the boundary line computed through the linear discriminant analysis (LDA) [64].

To test the proposed method in recognizing cells with LDs from the experimental QPMs, we consider another dataset made of monocytes THP-1 recorded before and after the appearance of LDs. In fact, within the WBCs, a remarkable increase in the number and size of LDs in response to stress conditions has been demonstrated [20]. For this reason, in order to promote the appearance of many and large LDs, no external agent was exploited, but monocytes population without LDs was left in culture for some days reducing the culture medium perfusion and thus inducing a stress condition. In particular, as summarized in Table 2, 864 QPMs related to 96 monocytes without LDs and 450 QPMs related to 50 monocytes with LDs have been considered. In Fig. 6(b), the same LDA boundary found in the lymphocytes vs. A2780 scatter plot has been exploited to recognize the presence of LDs inside monocytes. It is worth remarking that, although the LDA has been set on a different problem, also in this case the presence of LDs has been correctly identified in most of the experimental QPMs by only exploiting the perturbation that intracellular LDs introduce to the biolens features of the whole cell. In fact, in Fig. 6(b) we obtained an accuracy of 81.2% in detecting or not LDs inside the 1314 analyzed QPMs. Depending on the size and RI, LDs in some angular positions in 2D maps can be difficult to be detected or even non detectable at all. For example, the LDs can be occluded by the complexity

Biomedical Optics EXPRESS

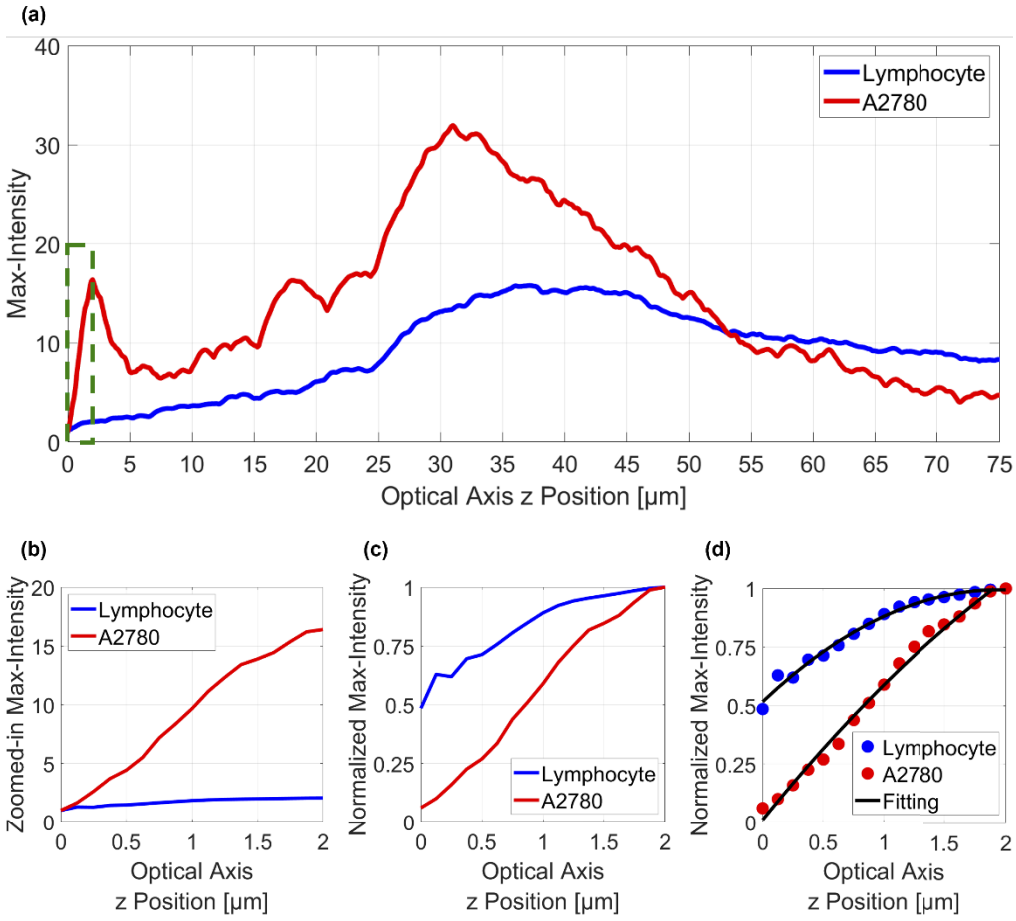

Fig. 5. Quantitative characterization of the alteration of the cell biolens features by LDs. (a) Comparison between the max-intensity curve of the Jurkat T-lymphocyte cell (blue line) and the A2780 cell (red line) analyzed in Fig. 2. **(b)** Zoom-in of the max-intensity curves in (a) in the [0,2] μm region (green box). **(c)** Zoomed-in max-intensity curves in (b) normalized to their maxima. **(d)** Normalized max-intensity curves (dots) with overlapped the 2nd order polynomial fitting (black line).

Biomedical Optics EXPRESS

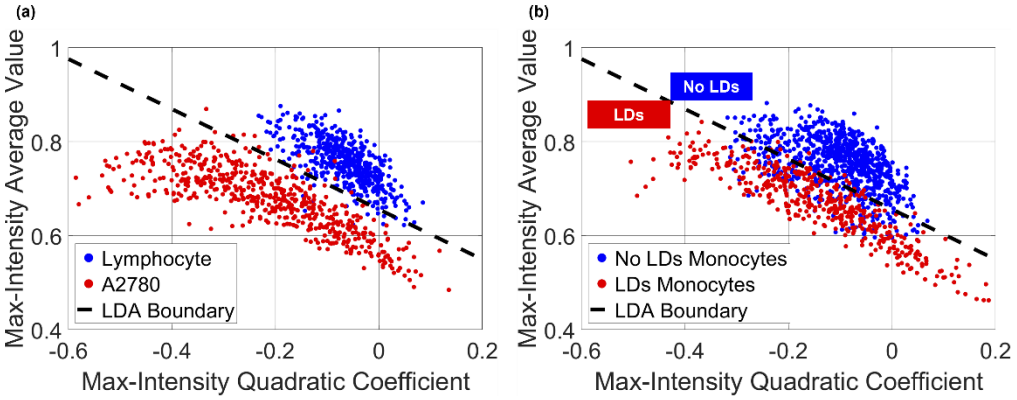

Fig. 6. Identification of cells with LDs from the in-flow QPMs represented through their max-intensity average values and quadratic coefficients. (a) Scatter plot of Jurkat T-lymphocyte (blue dots) vs. A2780 (red dots) cells, separated by the line boundary computed through the LDA (black line). **(b)** Scatter plot of monocytes without (blue dots) and with (red dots) LDs, separated by the LDA boundary found in (a).

of the nuclei's structure. A possible solution would be recording more than one QPM of the same cell during its rotation, as occurs in our system. In fact, cell rotation can allow to obtain one or more directions along which the LDs are more easily detectable, still without the need to retrieve the 3D RI tomograms.

Table 2. Dataset of monocytes THP-1 collected through the DH flow cytometer before and after the appearance of LDs

	# QPMs	# Cells
No LDs Monocyte	864	96
LDs Monocyte	450	50

For example, in our case study, as reported in Table 2, only 9 QPMs per cell have been recorded. Nevertheless, by using a max-voting strategy, remarkably the accuracy increases up to 100% in detecting or not LDs inside the 146 analyzed cells.

4. Conclusions

The investigation of functionalities and physio-pathologies related to LDs has boosted in the last years. LDs perform not only a simple fat reservoir role, but they have also a dynamic role in many cellular activities, e.g., defense activity against cellular stress condition and interaction with other intracellular organelles such as mitochondria and lysosomes. Therefore, it is important to having rapid tool for detecting their presence inside the living cells as biomarker to aid the diagnosis of LDs-related pathologies. In this work we went beyond the conventional biochemical and morphological analysis. We demonstrated that LDs can be rapidly detected by analyzing the focal properties of the whole cell. In fact, if we consider the cell as a biolens, the presence of LDs alters their lensing. By combining the availability of experimental in-flow TPM data with a proper numerical simulation we proved that the detection of LDs can be accomplished easily. The LDs are themselves biolenses and therefore the optical properties of the overall biological optical system consists in the whole cell (primary biolens) and the intracellular LDs (smaller biolens). Such system is a much more intricate optical system. Anyway we exploit the fact that

Biomedical Optics EXPRESS

the focal properties are significantly altered resulting in a detectable signature in the focusing characteristic of the biolens-system when LDs are present.

In our study we compared two different cell lines, i.e. A2780 ovarian cancer and Jurkat T-lymphocyte, and we showed that, thanks to the alteration of the cell biolens features due to LDs, their presence can be directly predicted from the 2D QPMs recorded in flow conditions. This means that the time and resource consuming tomographic reconstruction can be avoided if the sole detection is needed [55]. Moreover, we made other experiments where we considered a third cell line, i.e. human monocytes THP-1, recorded before and after the appearance of LDs. It is worth noting that the detection system here proposed could be further speeded up thanks to the employment of deep learning for a very fast QPM prediction from the recorded digital hologram [57]. As the results of our investigation characterize accurately the intracellular LDs, they can be useful for further applications as endogenous lensing for intracellular imaging [12]. Notice that, the proposed approach is focused on the identification of living cells having or not detectable LDs inside, i.e. without need to take into account the number and the size of LDs. A deeper characterization of the LDs distribution may be obtained by decoding the max-intensity curves behavior as a function of these information. Moreover, we expect that the detection accuracy of LDs could find benefit by adding other parameters not directly related to the biolens' features herein investigated. In summary, the study pave the way for additional perspectives on biolenses as well as the application of this concept for biomedical applications.

Acknowledgements. This work was partially supported at CNR-ISASI by project PRIN 2017, Morphological Biomarkers for early diagnosis in Oncology (MORFEO) Prot. 2017N7R2CJ.

Disclosures. The authors declare no conflicts of interest.

Data availability. Data underlying the results presented in this paper are not publicly available at this time but may be obtained from the authors upon reasonable request.

References

1. L. Miccio, P. Memmolo, F. Merola, P. A. Netti, and P. Ferraro, "Red blood cell as an adaptive optofluidic microlens," Nat. Commun. **6**(1), 6502 (2015).
2. L. Miccio, P. Memmolo, F. Merola, M. Mugnano, and P. Ferraro, "Optobiology: live cells in optics and photonics," JPhys Photonics **3**(1), 012003 (2020).
3. Y. Li, X. Liu, and B. Li, "Single-cell biomagnifier for optical nanoscopes and nanotweezers," Light: Sci. Appl. **8**(1), 61 (2019).
4. L. Miccio, J. Behal, M. Mugnano, P. Memmolo, B. Mandracchia, F. Merola, S. Grilli, and P. Ferraro, "Biological Lenses as a Photomask for Writing Laser Spots into Ferroelectric Crystals," ACS Appl. Bio Mater. **2**(11), 4675–4680 (2019).
5. N. Schuergers, T. Lenn, R. Kampmann, M. v Meissner, T. Esteves, M. Temerinac-Ott, J. G. Korvink, A. R. Lowe, C. W. Mullineaux, and A. Wilde, "Cyanobacteria use micro-optics to sense light direction," eLife **5**, 459 (2016).
6. P. Memmolo, F. Merola, L. Miccio, M. Mugnano, and P. Ferraro, "Investigation on dynamics of red blood cells through their behavior as biophotonic lenses," J. Biomed. Opt. **21**(12), 1 (2016).
7. F. Merola, Á. Barroso, L. Miccio, P. Memmolo, M. Mugnano, P. Ferraro, and C. Denz, "Biolens behavior of RBCs under optically-induced mechanical stress," Cytometry **91**(5), 527–533 (2017).
8. P. Memmolo, L. Miccio, F. Merola, M. Mugnano, and P. Ferraro, "Hydrodynamic red blood cells deformation by quantitative phase microscopy and Zernike polynomials," Front. Phys. **7**, 111 (2019).
9. Y. Li, X. Liu, X. Yang, H. Lei, Y. Zhang, and B. Li, "Enhancing upconversion fluorescence with a natural bio-microlens," ACS Nano **11**(11), 10672–10680 (2017).
10. P. Memmolo, L. Miccio, F. Merola, and P. Ferraro, "The Talbot effect in self-assembled red blood cells investigated by digital holography," JPhys Photonics **2**(3), 035005 (2020).
11. C. Jiang, H. Yue, B. Yan, B. Yan, B. Yan, T. Dong, X. Cui, P. Chen, P. Chen, and Z. Wang, "Label-free non-invasive subwavelength-resolution imaging using yeast cells as biological lenses," Biomed. Opt. Express **12**(11), 7113–7121 (2021).
12. X. Chen, T. Wu, Z. Gong, J. Guo, X. Liu, Y. Zhang, Y. Li, P. Ferraro, and B. Li, "Lipid droplets as endogenous intracellular microlenses," Light: Sci. Appl. **10**(1), 242 (2021).
13. X. Liu, Y. Li, X. Xu, Y. Zhang, and B. Li, "Red-blood-cell-based microlens: application to single-cell membrane imaging and stretching," ACS Appl. Bio Mater. **2**(7), 2889–2895 (2019).
14. B. Huang, H. Babcock, and X. Zhuang, "Breaking the diffraction barrier: super-resolution imaging of cells," Cell **143**(7), 1047–1058 (2010).

Biomedical Optics EXPRESS

15. L. Chen, Y. Zhou, R. Zhou, and M. H. Hong, "Microsphere – the future of optical microscopes," PhotonicsViews **18**(3), 79–81 (2021).
16. S.-Y. Cho, X. Gong, V. B. Koman, M. Kuehne, S. J. Moon, M. Son, T. T. S. Lew, P. Gordiichuk, X. Jin, H. D. Sikes, and M. S. Strano, "Cellular lensing and near infrared fluorescent nanosensor arrays to enable chemical efflux cytometry," Nat. Commun. **12**(1), 3079 (2021).
17. K. Kim, S. Lee, J. Yoon, J. Heo, C. Choi, and Y. Park, "Three-dimensional label-free imaging and quantification of lipid droplets in live hepatocytes," Sci. Rep. **6**(1), 36815 (2016).
18. D. J. Murphy, "The dynamic roles of intracellular lipid droplets: from archaea to mammals," Protoplasma **249**(3), 541–585 (2012).
19. J. Beuthan, O. Minet, J. Helfmann, M. Herrig, and G. Müller, "The spatial variation of the refractive index in biological cells," Phys. Med. Biol. **41**(3), 369–382 (1996).
20. J. A. Olzmann and P. Carvalho, "Dynamics and functions of lipid droplets," Nat. Rev. Mol. Cell Biol. **20**(3), 137–155 (2019).
21. M. A. Welte and A. P. Gould, "Lipid droplet functions beyond energy storage," Biochim. Biophys. Acta, Mol. Cell Biol. Lipids **1862**(10), 1260–1272 (2017).
22. H. Wu, P. Carvalho, and G. K. Voeltz, "Here, there, and everywhere: the importance of ER membrane contact sites," Science **361**(6401), 3563 (2018).
23. R. C. N. Melo and P. F. Weller, "Lipid droplets in leukocytes: organelles linked to inflammatory responses," Exp. Cell Res. **340**(2), 193–197 (2016).
24. F. Geltinger, L. Schartel, M. Wiederstein, J. Tevini, E. Aigner, T. K. Felder, and M. Rinnerthaler, "Friend or foe: lipid droplets as organelles for protein and lipid storage in cellular stress response, aging and disease," Molecules **25**(21), 5053 (2020).
25. Y. Imai, R. S. Cousins, S. Liu, B. M. Phelps, and J. A. Promes, "Connecting pancreatic islet lipid metabolism with insulin secretion and the development of type 2 diabetes," Ann. N. Y. Acad. Sci. **1461**(1), 53–72 (2020).
26. K. J. Williams and I. Tabas, "The response-to-retention hypothesis of early atherogenesis," Arterioscler., Thromb., Vasc. Biol. **15**(5), 551–561 (1995).
27. N. L. Gluchowski, M. Becuwe, T. C. Walther, and R. v. Farese, "Lipid droplets and liver disease: from basic biology to clinical implications," Nat. Rev. Gastroenterol. Hepatol. **14**(6), 343–355 (2017).
28. M. Bosch, M. Sánchez-Álvarez, A. Fajardo, R. Kapetanovic, B. Steiner, F. Dutra, L. Moreira, J. A. López, R. Campo, M. Marí, F. Morales-Paytuví, O. Tort, A. Gubern, R. M. Templin, J. E. B. Curson, N. Martel, C. Català, F. Lozano, F. Tebar, C. Enrich, J. Vázquez, M. A. del Pozo, M. J. Sweet, P. T. Bozza, S. P. Gross, R. G. Parton, and A. Pol, "Mammalian lipid droplets are innate immune hubs integrating cell metabolism and host defense," Science **370**(6514), eaay8085 (2020).
29. L. Liu, K. Zhang, H. Sandoval, S. Yamamoto, M. Jaiswal, E. Sanz, Z. Li, J. Hui, B. H. Graham, A. Quintana, and H. J. Bellen, "Glial lipid droplets and ros induced by mitochondrial defects promote neurodegeneration," Cell **160**(1-2), 177–190 (2015).
30. C. R. Santos and A. Schulze, "Lipid metabolism in cancer," FEBS J. **279**(15), 2610–2623 (2012).
31. A. L. S. Cruz, E. de A. Barreto, N. P. B. Fazolini, J. P. B. Viola, and P. T. Bozza, "Lipid droplets: platforms with multiple functions in cancer hallmarks," Cell Death Dis. **11**(2), 105 (2020).
32. L. Tirinato, F. Pagliari, T. Limongi, M. Marini, A. Falqui, J. Seco, P. Candeloro, C. Liberale, and E. di Fabrizio, "An Overview of Lipid Droplets in Cancer and Cancer Stem Cells," Stem Cells Int. **2017**, 1–17 (2017).
33. M. J. Thun, E. J. Jacobs, and C. Patrono, "The role of aspirin in cancer prevention," Nat. Rev. Clin. Oncol. **9**(5), 259–267 (2012).
34. P. T. Bozza, R. C. N. Melo, and C. Bandeira-Melo, "Leukocyte lipid bodies regulation and function: contribution to allergy and host defense," Pharmacol. Ther. **113**(1), 30–49 (2007).
35. M. H. den Brok, T. K. Raaijmakers, E. Collado-Camps, and G. J. Adema, "Lipid droplets as immune modulators in myeloid cells," Trends Immunol. **39**(5), 380–392 (2018).
36. E. A. Monson, A. M. Trenerry, J. L. Laws, J. M. Mackenzie, and K. J. Helbig, "Lipid droplets and lipid mediators in viral infection and immunity," FEMS Microbiol. Rev. **22**, 1732 (2021).
37. S. S. G. Dias, V. C. Soares, A. C. Ferreira, C. Q. Sacramento, N. Fintelman-Rodrigues, J. R. Temerozo, L. Teixeira, M. A. Nunes da Silva, E. Barreto, M. Mattos, C. S. de Freitas, I. G. Azevedo-Quintanilha, P. P. A. Manso, M. D. Miranda, M. M. Siqueira, E. D. Hottz, C. R. R. Pão, D. C. Bou-Habib, D. F. Barreto-Vieira, F. A. Bozza, T. M. L. Souza, and P. T. Bozza, "Lipid droplets fuel SARS-CoV-2 replication and production of inflammatory mediators," PLoS Pathog. **16**(12), e1009127 (2020).
38. R. Nardacci, F. Colavita, C. Castilletti, D. Lapa, G. Matusali, S. Meschi, F. del Nonno, D. Colombo, M. R. Capobianchi, A. Zumla, G. Ippolito, M. Piacentini, and L. Falasca, "Evidences for lipid involvement in SARS-CoV-2 cytopathogenesis," Cell Death Dis. **12**(3), 263 (2021).
39. A. S. Martins, I. C. Martins, and N. C. Santos, "Methods for lipid droplet biophysical characterization in flaviviridae infections," Front. Microbiol. **9**, 1043 (2018).
40. T. Fam, A. Klymchenko, and M. Collot, "Recent advances in fluorescent probes for lipid droplets," Materials **11**(9), 1768 (2018).
41. Y. Suzuki, K. Kobayashi, Y. Wakisaka, D. Deng, S. Tanaka, C.-J. Huang, C. Lei, C.-W. Sun, H. Liu, Y. Fujiwaki, S. Lee, A. Isozaki, Y. Kasai, T. Hayakawa, S. Sakuma, F. Arai, K. Koizumi, H. Tezuka, M. Inaba, K. Hiraki, T. Ito, M.

Biomedical Optics EXPRESS

Hase, S. Matsusaka, K. Shiba, K. Suga, M. Nishikawa, M. Jona, Y. Yatomi, Y. Yalikun, Y. Tanaka, T. Sugimura, N. Nitta, K. Goda, and Y. Ozeki, "Label-free chemical imaging flow cytometry by high-speed multicolor stimulated Raman scattering," Proc. Natl. Acad. Sci. **116**(32), 15842–15848 (2019).
42. B. Guo, C. Lei, H. Kobayashi, T. Ito, Y. Yalikun, Y. Jiang, Y. Tanaka, Y. Ozeki, and K. Goda, "High-throughput, label-free, single-cell, microalgal lipid screening by machine-learning-equipped optofluidic time-stretch quantitative phase microscopy," Cytometry Part A **91**(5), 494–502 (2017).
43. K. C. M. Lee, M. Wang, K. S. E. Cheah, G. C. F. Chan, H. K. H. So, K. K. Y. Wong, and K. K. Tsia, "Quantitative phase imaging flow cytometry for ultra-large-scale single-cell biophysical phenotyping," Cytometry Part A **95**(5), 510–520 (2019).
44. K. C. M. Lee, A. K. S. Lau, A. H. L. Tang, M. Wang, A. T. Y. Mok, B. M. F. Chung, W. Yan, H. C. Shum, K. S. E. Cheah, G. C. F. Chan, H. K. H. So, K. K. Y. Wong, and K. K. Tsia, "Multi-ATOM: Ultrahigh-throughput single-cell quantitative phase imaging with subcellular resolution," J. Biophotonics **12**(7), 1 (2019).
45. Y. Wu, Y. Zhou, C.-J. Huang, H. Kobayashi, S. Yan, Y. Ozeki, Y. Wu, C.-W. Sun, A. Yasumoto, Y. Yatomi, C. Lei, and K. Goda, "Intelligent frequency-shifted optofluidic time-stretch quantitative phase imaging," Opt. Express **28**(1), 519 (2020).
46. M. K. Kim, "Principles and techniques of digital holographic microscopy," J. Photonics Energy **A197**, 018005 (2010).
47. J. Min, B. Yao, V. Trendafilova, S. Ketelhut, L. Kastl, B. Greve, and B. Kemper, "Quantitative phase imaging of cells in a flow cytometry arrangement utilizing Michelson interferometer-based off-axis digital holographic microscopy," J. Biophotonics **12**(9), 1344 (2019).
48. Y. Park, C. Depeursinge, and G. Popescu, "Quantitative phase imaging in biomedicine," Nat. Photonics **12**(10), 578–589 (2018).
49. W. Choi, C. Fang-Yen, K. Badizadegan, S. Oh, N. Lue, R. R. Dasari, and M. S. Feld, "Tomographic phase microscopy," Nat. Methods **4**(9), 717–719 (2007).
50. Z. Wang, V. Bianco, D. Pirone, P. Memmolo, M. M. Villone, P. L. Maffettone, and P. Ferraro, "Dehydration of plant cells shoves nuclei rotation allowing for 3D phase-contrast tomography," Light: Sci. Appl. **10**(1), 187 (2021).
51. F. Merola, P. Memmolo, L. Miccio, R. Savoia, M. Mugnano, A. Fontana, G. D'Ippolito, A. Sardo, A. Iolascon, A. Gambale, and P. Ferraro, "Tomographic flow cytometry by digital holography," Light: Sci. Appl. **6**(4), e16241 (2017).
52. M. M. Villone, P. Memmolo, F. Merola, M. Mugnano, L. Miccio, P. L. Maffettone, and P. Ferraro, "Full-angle tomographic phase microscopy of flowing quasi-spherical cells," Lab Chip **18**(1), 126–131 (2018).
53. D. Pirone, P. Memmolo, F. Merola, L. Miccio, M. Mugnano, A. Capozzoli, C. Curcio, A. Liseno, and P. Ferraro, "Rolling angle recovery of flowing cells in holographic tomography exploiting the phase similarity," Appl. Opt. **60**(4), A277 (2021).
54. D. Pirone, M. Mugnano, P. Memmolo, F. Merola, G. C. Lama, R. Castaldo, L. Miccio, V. Bianco, S. Grilli, and P. Ferraro, "Three-dimensional quantitative intracellular visualization of graphene oxide nanoparticles by tomographic flow cytometry," Nano Lett. **21**(14), 5958–5966 (2021).
55. D. Pirone, D. Sirico, L. Miccio, V. Bianco, M. Mugnano, D. del Giudice, G. Pasquinelli, S. Valente, S. Lemma, L. Iommarini, I. Kurelac, P. Memmolo, and P. Ferraro, "Lipid droplets 3D full measurement by holographic in-flow tomography," bioRxiv 2021.12.09.471789 (2021).
56. D. Howie, A. ten Bokum, A. S. Necula, S. P. Cobbold, and H. Waldmann, "The role of lipid metabolism in T lymphocyte differentiation and survival," Front. Immunol. **8**, 1949 (2018).
57. D. Pirone, D. Sirico, L. Miccio, V. Bianco, M. Mugnano, P. Ferraro, and P. Memmolo, "Speeding up reconstruction of 3D tomograms in holographic flow cytometry via deep learning," Lab Chip **22**(4), 793–804 (2022).
58. C. J. Mann and M. K. Kim, "Quantitative phase-contrast microscopy by angular spectrum digital holography," Proc. SPIE **6090**, 60900B (2006).
59. P. Memmolo, L. Miccio, M. Paturzo, G. di Caprio, G. Coppola, P. A. Netti, P. Ferraro, G. di Caprio, L. Miccio, M. Paturzo, P. A. Netti, and P. Ferraro, "Recent advances in holographic 3D particle tracking," Adv. Opt. Photonics **7**(4), 713–755 (2015).
60. D. G. Sirico, L. Miccio, Z. Wang, P. Memmolo, W. Xiao, L. Che, L. Xin, F. Pan, and P. Ferraro, "Compensation of aberrations in holographic microscopes: main strategies and applications," Applied Physics B 2022 **128**(4), 1–19 (2022).
61. Q. Kemao, "Windowed Fourier transform for fringe pattern analysis," Appl. Opt. **43**(13), 2695 (2004).
62. J. M. Bioucas-Dias and G. Valadao, "Phase unwrapping via graph cuts," IEEE Trans. on Image Process. **16**(3), 698–709 (2007).
63. S. Chowdhury, M. Chen, R. Eckert, D. Ren, F. Wu, N. Repina, and L. Waller, "High-resolution 3D refractive index microscopy of multiple-scattering samples from intensity images," Optica **6**(9), 1211 (2019).
64. A. J. Izenman, *Modern Multivariate Statistical Techniques* (Springer New York, 2008).